Materials Chemistry

PAPER

Top-down synthesis of multifunctional iron oxide nanoparticles for macrophage labelling and manipulation†

Vincenzo Amendola,*[a] Moreno Meneghetti,[a] Gaetano Granozzi,[a] Stefano Agnoli,[a] Stefano Polizzi,[b] Pietro Riello,[b] Anita Boscaini,[c] Cristina Anselmi,[c] Giulio Fracasso,[c] Marco Colombatti,[c] Claudia Innocenti,[d] Dante Gatteschi[d] and Claudio Sangregorio[de]

Multifunctional iron oxide (FeOx) magnetic nanoparticles (MNPs) are promising items for biomedical applications. They are studied as theranostic agents for cancer treatment, selective probes for bioanalytical assays, controllable carriers for drug delivery and biocompatible tools for cell sorting or tissue repair. Here we report a new method for the synthesis in water of FeOx–MNPs *via* a top-down physical technique consisting in Laser Ablation Synthesis in Solution (LASiS). LASiS is a green method that does not require chemicals or stabilizers, because nanoparticles are directly obtained in water as a stable colloidal system. A gamut of characterization techniques was used for investigating the structure of FeOx–MNPs that have a polycrystalline structure prevalently composed of magnetite (*ca.* 75%) and hematite (*ca.* 22%). The FeOx–MNPs exhibit very good magnetic properties if compared to what is usually reported for iron oxide nanoparticles, with saturation magnetization close to the bulk value (*ca.* 80 emu g^{-1}) and typical signatures of the coexistence of ferrimagnetic and antiferromagnetic phases in the same particle. The functionalization of FeOx–MNPs after the synthesis was possible with a variety of ligands. In particular, we succeeded in the functionalization of FeOx–MNPs with carboxylated phosphonates, fluorescent alkylamines, fluorescent isothiocyanates and bovine serum albumin. Our FeOx–MNPs showed excellent biocompatibility. Multifunctional FeOx–MNPs were exploited for macrophage cell labelling with fluorescent probes as well as for cell sorting and manipulation by external magnetic fields.

Introduction

Iron oxide (FeOx) magnetic nanoparticles (MNPs) find applications in several branches of technology like biomedicine, environmental sciences, information storage, micromechanics and microfluidics.[1–3] In the field of nanomedicine there is a growing interest due to the intrinsic multifunctionality of MNPs.[3,4] For example, they can be used as negative contrast agents in magnetic resonance imaging (MRI)[5,6] or for an imaging technique with higher resolution called magnetic particle imaging (MPI).[7] MNPs are also studied as therapeutic agents for radio-frequency magnetic field induced hyperthermia of malignant tissues and for fast tissues cicatrization.[4,8] Recently, a technique for destroying cancer cells based on magnetic field induced mechanical damage of functionalized magnetic discs was also proposed.[9] Moreover, MNPs can be directed to specific sites by an external magnetic field for drug delivery and theranostic purposes.[4,10] Alternatively, they can be used for driving a distinct object to a predetermined site, like in cell sorting and cell manipulation as well as in toxin decoration.[3,4,10]

Controlling the surface chemistry of MNPs is a crucial point for introducing other functionalities. Stabilizing shells based on stealth polymers or polysaccharides are useful for improving the stability in physiological medium and for escaping the reticulo-endothelial system, in order to allow targeting and diffusion in remote parts of the body.[4,5] Optical probes like fluorescent molecules can be useful for improving the resolution of MRI and can be used for intrasurgical imaging.[11,12] Antibodies and other targeting functionalities (*e.g.* folic acid) can confer high selectivity to particle accumulation that cannot be obtained by external magnetic fields.[13–15] In recent years, however, effective

[a]Department of Chemical Sciences, University of Padova, via Marzolo 1, I-35131 Padova, Italy. E-mail: vincenzo.amendola@unipd.it

[b]Department of Molecular Sciences and Nanosystems Università Cà Foscari Venezia and INSTM UdR Venezia, via Torino 155/b, I-30172 Venezia-Mestre, Italy

[c]Department of Pathology and Diagnostic, Section of Immunology, University of Verona, P.le L.A. Scuro 10, I-37134 Verona, Italy

[d]INSTM RU and Department of Chemistry, University of Florence, via della Lastruccia 3, 50019 Sesto F.no, FI, Italy

[e]CNR-ISTM Milano, via C. Golgi 19, 20133 Milano, Italy

targeting of tissues for imaging or therapy was mainly obtained by the enhanced permeation and retention (EPR) effect,[3,6,14,16,17] by the preferential accumulation of magnetic nanoparticles in Kupffer cells in the liver[3,6] or by using the ability of macrophages and stem cells in infiltrating deep tissues, with or without the guide of an external magnetic field.[5,16,18,19] In all cases, important requirements are high biocompatibility, good magnetic properties, an average size above kidneys clearance threshold and a surface chemistry allowing particles uptake in the desired sites.[3,4]

Within the reported context, FeOx–MNPs offer some advantages in comparison to other MNPs due to their good biocompatibility and long term biodegradability. The standard preparation methods of FeOx–MNPs consist in a wet chemistry bottom up approach in water or organic solvents.[4,10] Due to the assistance of stabilizers, wet chemistry methods allow a good control of particles size and polydispersity at the nanometric scale.[4,10] Further functionalization or stabilization of particles is possible by procedures like place exchange, silanization and *in situ* or *ex situ* polymer encapsulation.[4,10,20,21]

However, wet chemistry methods can have some drawbacks. Some approaches for the synthesis in organic solvents can involve expensive chemicals (*e.g.* the organometallic precursors) and can require high temperature and pressure, therefore they cannot be considered as "green" methods.[13,22,23] For biomedical applications, nanoparticles must become hydrophilic by replacing the hydrophobic shell.[4,10,24] Some concerns about the biocompatibility of FeOx particles obtained in organic solvents also exist.[10,22] On the other hand, the synthesis in water usually is more problematic for the control of particle crystallinity *versus* the amorphous fraction and for the selectivity of the oxide phase.[5,23] In order to obtain magnetite Fe_3O_4-MNPs with the correct stoichiometry and, hopefully, with high crystallinity, the solution must be kept under nitrogen or argon atmosphere because of the fast oxidation of Fe(II) by atmospheric oxygen.[25] Sometimes also high temperatures and pressures are required, as in the hydrothermal synthesis.[22,23,25,26] In most cases, the synthesis of FeOx–MNPs with saturation magnetization of the order of 50–65 emu g^{-1} was reported, depending on particles size, in contrast to a value of *ca.* 92 emu g^{-1} for bulk magnetite.[4] Lower values of saturation magnetization can be due to finite size effects like spin canting,[27,28] to the presence of a dead spin layer,[29] and to amorphous phases or to oxide phases with inferior magnetic properties like hematite (α-Fe$_2$O$_3$).[10,30]

In recent years some efforts have been directed to obtain FeOx–MNPs with higher saturation magnetization by environmental friendly procedures.[13,22,25,26,31] In particular, bacterial production of FeOx–MNPs and flame synthesis showed to be viable green techniques for obtaining nanoparticles with high saturation magnetization, but there are some problems for particles functionalization and dispersion.[22,32,33]

Here we report about a top-down approach for the synthesis of FeOx–MNPs by a physical method called Laser Ablation Synthesis in Solution (LASiS), consisting in the laser ablation of a bulk iron target in aqueous solution. The so obtained FeOx–MNPs form a colloidal system that is stable in water for a long time even in the absence of stabilizers. Moreover, LASiS is a green approach to the synthesis of nanomaterials and requires limited manual operation.[34] In the present work, using a gamut

of complementary characterization techniques, we demonstrate that our synthetic procedure originates polycrystalline ultrasmall FeOx–MNPs, prevalently composed of magnetite (*ca.* 75%) showing a saturation magnetization comparable to the bulk one (*ca.* 80 emu g^{-1}). Moreover, the functionalization of FeOx–MNPs was possible by straightforward procedures with a variety of ligands like fluorescent alkylamines, fluorescent isothiocyanates, bovine serum albumin and stabilizing carboxylated phosphonates. In particular, the multifunctionalization of FeOx–MNPs by sequential addition of ligands was demonstrated by using two different coordinating functionalities bound to two different fluorescent probes.

Our multifunctional FeOx–MNPs were used for fluorescent labelling of macrophage cells and for cell sorting and cell manipulation studies by external magnetic fields with high efficiency. Magneto-fluorescent macrophage cells are of great interest in nanomedicine because they can act as carriers of MNPs into deep lesions, aiming at the multimodal magnetic resonance–fluorescence imaging and at magnetic field induced hyperthermia.

Experimental methods

Synthetic procedure

FeOx–MNPs were obtained by Laser Ablation Synthesis in Solution (LASiS), by a procedure similar to what previously reported.[34–36] Briefly, laser ablation was obtained with Nd:YAG (Quantel YG981E) laser pulses at 1064 nm (9 ns) focused with a 10 cm focus lens on a 99.99% pure iron plate placed at the bottom of a cell containing bidistilled water. Pulses of 10 J cm^{-2} at a 10 Hz repetition rate for 90 min were employed. Disodium ethylenediaminetetraacetate (>98%, Sigma Aldrich) was added with a 5 mM final concentration to the so obtained FeOx–MNPs solution and heated at 55 °C for 60′. Particles were washed multiple times with bi-distilled water by centrifugation at 5000 rpm.

Structural characterization

For transmission electron microscopy (TEM) we collected the images at 300 kV with a JEOL JEM 3010 microscope equipped with a Gatan Multiscan CCD Camera model 794. The samples for TEM analysis were prepared by evaporating FeOx–MNPs suspension on a copper grid covered with a holey amorphous carbon film. The micro-Raman measurements were recorded by focusing the 5× objective of a Renishaw inVia micro-Raman instrument on a dried powder of FeOx–MNPs using the 633 nm line of an He–Ne laser with an output power of 0.75 mW. At high laser power the oxidation of magnetite to hematite was observed. For UV-visible spectroscopy we used a Varian Cary 5 spectrometer and 2 mm optical path quartz cells. FTIR measurements were recorded in attenuated total refraction (ATR) configuration on a Ge head with a Nicolet 5700 spectrophotometer on dried FeOx–MNP powders. DLS measurements were performed with a SpectraPhysics Nicomp 380 instrument (Particle Sizing Systems, Santa Barbara, CA) equipped with a 633 nm He–Ne laser. We reported the number weighted size distribution and relative standard deviation because the results were in good agreement with what observed by TEM analysis on the same samples.

A Philips diffractometer was employed to collect the XRD patterns. The setup is constituted by an X'Pert vertical goniometer with Bragg–Brentano geometry, a focusing graphite monochromator and a proportional counter with a pulse-height discriminator and it is connected to a highly stabilized generator. Nickel-filtered Cu Kα radiation and a step-by-step technique are employed (steps of $2\theta = 0.05°$), with collection times of 30 s per step. Line broadening analysis (LBA) was carried out using a previously published method.[37] The quantitative phase analysis by X-ray diffraction was performed using the Rietveld method (DBWS9600 computer program written by Sakthivel and Young and modified by Riello *et al.*)[38] and according to the following PDF files: Fe Pdf: 87-722; FeO Pdf: 75-1550; Fe_2O_3 Pdf: 33-664; Fe_3O_4 Pdf: 89-688. The Fe peak corresponds to particles with a size of *ca.* 60 nm as obtained by the Debye–Scherrer formula that were not observed in TEM images.

For XPS measurements, a droplet of a solution containing the FeOx–MNPs has been let dry off on a roughened tantalum sample holder until obtaining a very thin homogeneous film. The surface composition of the FeOx–MNP powders was analyzed by XPS using a modified VG ESCALAB MKII (Vacuum generators, Hastings, England) equipped with a twin (Mg/Al) anode X-ray source, a sputter gun, and a hemispherical electrostatic analyzer with a five channel detector. The XPS data reported in the present study were obtained using Al-Kα radiation (1486.6 eV) as an excitation source. Photoemission spectra have been obtained at room temperature using a normal emission geometry. Prior to measurements, the samples were degassed overnight in the analysis chamber (pressure lower than 10^{-8} mbar).

For fluorescence analysis we used a Perkin Elmer LS50B luminescence spectrometer and 1 cm quartz cells.

The Fe content in our samples was determined by inductively coupled plasma-mass spectrometry (ICP-MS) measurements carried out with a Thermo Elemental X7 Series instrument equipped with the PlasmaLab software package. For instrument calibration, a standard Fe solution was purchased from Spectrascan. The iron concentration of a series of reference solutions was determined by ICP-MS and then correlated to the absorption spectrum of these solutions.

Magnetic characterization

The magnetic properties of these samples were investigated both in solution and as dry powder using a Cryogenic S600 SQUID magnetometer; Zero-field-cooled (ZFC) magnetizations were measured by cooling samples in zero magnetic field and then by increasing the temperature in an applied field of 50 Oe, while field-cooled (FC) curves were recorded by cooling the samples in the same probe field. The field dependence of the magnetization (hysteresis loop) was recorded up to ±50 or ±65 kOe at $T = 2.5$ K. When possible the saturation magnetization (M_s) was derived from a plot of M *versus* $1/H$, extrapolating the M values for $1/H \rightarrow 0$. The content of iron in sample solutions was determined by ICP-MS analysis on aliquots of the same solutions used for the measurements.

Functionalization

Functionalization by adding the ligands after the synthetic procedure consisted in the addition of a 0.01% in weight aqueous solution of BSA or F-BSA (Fatty Acid Free Bovine Serum Albumin or Albumin–fluorescein isothiocyanate conjugate from Sigma Aldrich) and 0.005% aqueous solutions of F–PEG–NH2 (Fluorescein–PEG–Amine, M_w 5000, from Lysan Bio), FITC (fluorescein isothiocyanate mixed isomers from Sigma Aldrich), TRITC (Tetramethylrhodamine isothiocyanate mixed isomers from Sigma Aldrich) or PMIDA (*N*-phosphonomethyl iminodiacetic acid hydrate from Sigma Aldrich) to an equal volume of FeOx–MNPs in water (0.5 mg per ml iron). We tested various pH conditions by incubating the FeOx–MNPs with the ligands at acidic (pH 4) or basic (pH 9) conditions and we found that the best conjugation efficiency was obtained in acidic pH. This is likely due to the good stability of FeOx–MNPs observed at acidic pH, as proved also by DLS measurements. In order to prevent the adsorption of carboxylic or phosphate molecules on particles surface, the pH was set by adding controlled amounts of very diluted HCl or NaOH solutions. After 24 hours of incubation at room temperature, the solutions were washed at least twice by centrifugation at 5000 rpm with bidistilled water and twice with 5 mM PBS solution.

Cell labelling and manipulation

U937 cells were obtained from the American Type Culture Collection (ATCC) and maintained according to ATCC protocols. The human non-adherent monocyte-like U937 cells were differentiated into macrophages by a 48 hour exposure to PMA (phorbol 12-myristate 13-acetate, Sigma-Aldrich) at a concentration of 40 nM. At day 0 cells were seeded at 0.5×10^6 cells per well in a 6 well plate and treated with PMA; after 48 hours the medium was changed and the cells resuspended in complete medium without PMA. At day 3 the uptake experiments were performed; briefly, cells were incubated in complete medium at 37 °C for 4 hours with F–PEG–NH$_2$/FeOx–MNPs equivalent to a final concentration of 0.36 mg per ml of iron. A mock-treated control well was also prepared. For flow cytometry analysis, each well was washed four times with PBS at the end of the incubation period to eliminate the non-internalized FeOx–MNP; adherent cells were detached with the trypsin/EDTA solution and washed three times with PBS. Two samples, one of FeOx–MNPs treated and one of non-treated cells, were also stained for 30 minutes at 0 °C with APC anti-human CD13 (BD Biosciences Pharmingen, NY, US) and washed three times with ice cold PBS. CD13-stained and non-stained cells were analyzed using a BD FACS-Canto cytometer; an aliquot of analyzed cells were used in the magnetic cell sorting experiments. Magnetic separation of FeOx–MNP tracked cells was performed at 4 °C; after a 10 minute exposure to a magnetic field non-attracted cells were washed out. Magnetic sorted and non-attracted cells were re-analyzed by flow cytometry.

For confocal microscopy analysis U937 cells seeded in a 24 well plate on polylysine coated glass slides were differentiated into macrophages and were treated with FeOx–MNPs as previously described. After washing of non-internalized FeOx–MNPs, cells were fixed in 2% paraformaldehyde, washed four times with PBS and stained with APC anti-human CD13. Glass slides were washed in PBS and mounted for confocal microscopy analysis (Zeiss LSM 510 confocal microscope).

Cell viability after FeOx–MNPs incorporation was evaluated by the XTT assay. Briefly, U937 differentiated cells were obtained according to the above described protocol and treated with FeOx–MNPs at 37 °C for 4 hours at a final iron concentration of 0.18, 0.36 and 0.72 mg ml^{-1}. Then, the cells were washed to remove FeOx–MNPs and the medium was replaced. After 20 hours, the cell viability was measured with an XTT assay.

Cell apoptosis was assessed by the human Annexin V-FITC Kit (Bender MedSystems, Wien, Austria). Cells were incubated with FeOx–MNPs at 37 °C for 4 hours (iron concentration of 0.36 mg ml^{-1}), then washed to remove excess FeOx–MNPs and the medium was replaced. After 2 h and 20 h, cells were treated with the human Annexin V-FITC Kit and analysed with flow cytometry.

Results and discussion

Synthesis and characterization

FeOx–MNPs were obtained by a top-down physical method consisting in the Laser Ablation Synthesis in Solution (LASiS) of a bulk iron (99.99%) target in water. LASiS is a straightforward procedure that requires a simple experimental setup and can be applied to the synthesis of a variety of nanostructured materials by operating minor changes in the experimental conditions.[34] The synthesis of FeOx–MNPs by LASiS in water mimics the procedure successfully applied to the synthesis of noble metal nanoparticles in similar conditions.[34–36,39,40] Laser ablation was carried out with laser pulses at 1064 nm (9 ns, 10 Hz, 10 J cm^{-2}) of a Nd:YAG laser focused on a pure iron plate placed at the bottom of a cell containing bidistilled water. Except bulk iron and water, no other chemicals or stabilizers are required by LASiS. By ICP-MS analysis, we quantified the yield of FeOx–MNPs obtained by LASiS in about 1 mg per 80 000 laser pulses at 1064 nm (9 ns, 10 J cm^{-2}). These figures correspond to 0.45 mg h^{-1} at 10 Hz and 45 mg h^{-1} at 1 kHz, therefore LASiS of FeOx–MNPs has the potential to be scaled up to gram scale synthesis by optimizing the experimental setup and the ablation parameters, in order to obtain synthetic yields comparable to other methods like chemical reduction or spray pyrolysis.

Transmission electron microscope (TEM) analysis showed that FeOx–MNPs have sizes in the 5–30 nm range with a log-normal size distribution, an average size of 10 ± 6 nm and a well defined spherical shape (Fig. 1a and b). High resolution TEM (HRTEM) analysis clearly evidenced the polycrystalline structure of the nanoparticles, with crystallite size on the order of 3–5 nm (Fig. 1c). This finding is in agreement with nanoparticle formation mechanism usually observed with LASiS, consisting in the nucleation of small embryos followed by their coalescence into larger particles.[34] The HRTEM analysis evidenced the formation of nanocrystals with prevailing crystalline interplanar distances of 0.25 nm and 0.48 nm (Fig. 1c). Within the experimental error, these distances are compatible with iron oxide phases like magnetite or maghemite (0.25 and 0.48 nm for (311) and (111) planes respectively) and hematite (0.25 nm for (110) planes), but not with metallic iron (0.20 nm for (110) planes).[30] This is in agreement with what expected, because the ablation process produces a plasma plume rich of
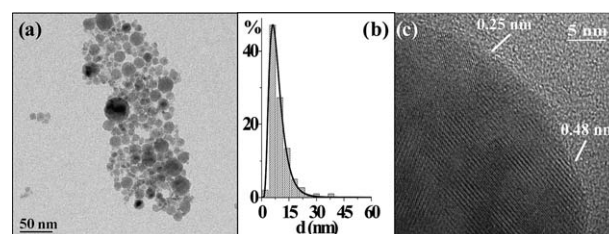
Fig. 1 TEM images of FeOx–MNPs. The particle size is in the 5–30 nm range (a) with a log-normal size distribution, as reported in the histogram (b), with an average of 10 nm and a standard deviation of 6 nm. The HRTEM image (c) shows a polycrystalline structure. We measured interplanar distances of 0.25 nm that matches with magnetite/maghemite (311) or hematite (110), and of 0.48 nm that matches with magnetite/maghemite (111) planes.

iron atoms coming from the target as well as of reactive oxygen species coming from the water solution.[34] Due to the polycrystalline structure and to the fast formation kinetics of FeOx–MNPs, grain boundaries are highly defective, though no amorphous domains are observed inside the particles. We also found that LASiS produced a fraction of amorphous material present as a network with micrometric size, probably due to iron hydrates. For this reason, the FeOx–MNPs solution obtained by LASiS were washed with 5 mM disodium ethylenediaminetetraacetate (EDTA) at 55 °C for 60′ in order to selectively remove the amorphous fraction, according to a well established procedure.[41]

The determination of the iron oxide phases composing the FeOx–MNPs is not a straightforward task, because some oxide phases have similar structural parameters but not necessarily identical magnetic properties.[30] Therefore we used a series of investigation techniques that provided complementary information about nanoparticles composition.

Raman spectroscopy is useful for the identification of the iron oxide phase because magnetite, maghemite and hematite have different Raman active vibrational fingerprints, although the Raman bands proper to FeOx phases may not always be observed when crystalline grains have sizes of the order of 3–5 nm.[42,43] In our case, the spectrum collected on a dried FeOx–MNPs sample with the 633 nm He–Ne laser line of a micro-Raman spectrometer (Fig. 2a) shows one peak at 670 cm^{-1} that matches with the Raman spectrum of magnetite reported in the literature. Since no traces are present from other bands like those proper to maghemite or hematite, one can suppose that magnetite is the prevailing phase in our sample.[42]

UV-visible spectroscopy can be useful for identifying iron oxide phases because only magnetite shows a broad absorption band in the near infrared region due to intervalence charge transfer transitions.[44] The UV-visible spectrum of FeOx–MNPs in water solution (Fig. 2b) clearly shows a band at wavelengths longer than 800 nm that is proper to magnetite and a more intense absorption edge at shorter wavelengths that is not distinctive of the iron oxide phase.[44]

Fourier transformed infrared (FTIR) spectroscopy is useful for evidencing the presence of magnetite and maghemite in the FeOx–MNPs sample, because maghemite is characterized by a peak close to 600 cm^{-1}, while magnetite has a strong IR
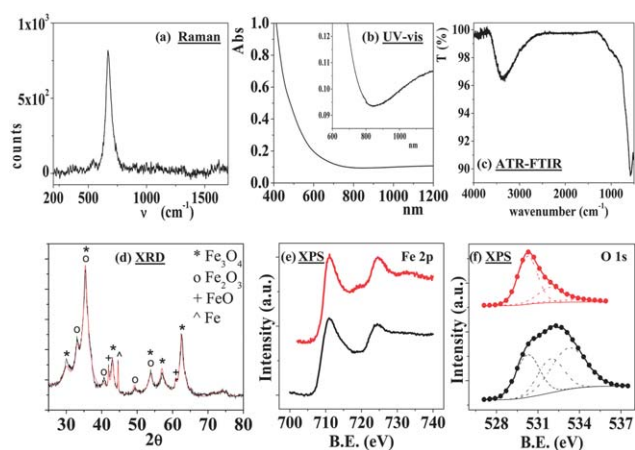
Fig. 2 (a) Raman spectrum on dried FeOx–MNPs showing a sharp peak at 670 cm^{-1} and a weak band at 540 cm^{-1} typical of magnetite. (b) UV-visible spectrum of FeOx–MNPs solution after the synthetic procedure showing the absorption edge at small wavelengths proper to iron oxides and the large absorption band over 800 nm characteristic of magnetite. The inset shows a magnification of the absorption band in the near infrared range. (c) ATR–FTIR spectrum of dried FeOx–MNP powders showing a sharp absorption band at 570 cm^{-1} proper to magnetite, while no other bands are observed, indicating that no other contaminants are present in the sample. (d) Powder XRD analysis of FeOx–MNPs (black line) and Rietveld fitting (red line). Magnetite is the prevailing component (ca. 75%), with ca. 22% of hematite, ca. 2% of wuestite and ca. 1% of metallic iron. (e and f) XPS data (Al-Kα) in the Fe 2p and O 1s regions collected on a FeOx–MNPs sample (black line) and on commercial 5 μm magnetite particles (red line).

absorption band at 570 cm^{-1}.[10,45–48] In the present case, the FTIR spectrum (Fig. 2c) is dominated by the absorption band of magnetite at 570 cm^{-1}, while a shoulder is observed at longer wavenumbers that can be attributed to traces of maghemite or to defective FeOx phases like nanostructured hematite.[10,45–49] As a further confirmation, we observed the same band at 570 cm^{-1} also in the spectrum of a reference commercial magnetite sample (5 μm particles). The FTIR spectrum has been collected in the whole analysis range of 500–4000 cm^{-1} allowed by the Ge head in the ATR configuration, to show that no vibrations ascribable to organic contaminants are present. This finding confirms that our synthetic procedure based on LASiS allows the synthesis of FeOx–MNPs that are free of chemical by-products.

X-Ray diffraction (XRD) was performed on FeOx–MNPs for obtaining a complete identification of the phases composing the particles (Fig. 2d). The reflections of magnetite and maghemite cannot be easily discriminated by XRD.[30,50] However, the results of the previous characterization techniques indicated that magnetite should be the prevailing phase in our samples. By the Rietveld analysis of the spectrum, we evaluated that the cubic spinel phase ascribable to the magnetite Fe$_3$O$_4$ is the prevailing phase ($\sim$75% in weight), with a fraction of hematite α-Fe$_2$O$_3$ ($\sim$22%), traces of wuestite FeO ($\sim$2%) and iron Fe ($\sim$1%). The Rietveld analysis indicated that crystalline domains are 3–5 nm in size, in agreement with the polycrystalline structure observed by HRTEM. The refined lattice parameter of the spinel phase is 0.8382 ± 0.0006 nm, closer to the magnetite than to the maghemite cell (0.8396 and 0.8352 respectively), in agreement

with the other experimental evidence that the FeOx–MNPs are composed of magnetite.

Since surface chemical properties of the FeOx–MNPs are important for the successive functionalization, X-ray photoelectron spectroscopy (XPS) measurements were performed in order to obtain information about the surface composition. In Fig. 2d and e we report the Fe 2p and O 1s XPS regions collected on our FeOx–MNPs, together with the corresponding data of a reference commercial magnetite sample (5 μm particles). The Fe 2p photoemission line (Fig. 2d) measured on the FeOx–MNPs presents broader features with respect to the commercial magnetite standard: even if the overall shape and energy position (Fe 2p$_{3/2}$ maximum at 711 eV) of the two spectra are very similar, one can observe that, in the case of the spectrum of the FeOx–NPs, the full width at half maximum (FWHM) of the peaks is larger (5 eV vs. 4 eV) and the distinctive satellite at 8.5 eV from the main 2p$_{3/2}$ peak, typical of stoichiometric magnetite, is missing.[51] These findings suggest that the surface of our FeOx–MNPs is composed by a mixture of FeOx phases beside to the prevalent magnetite that explains the slight broadening of the main photoemission line on the low energy side and the absence of a sharp satellite, and of Fe$_2$O$_3$ and hydroxide FeOOH, which determines the slight enlargement of the photoemission peak on the high energy slope. On the other hand, there is no indication of the presence of metal Fe in the surface region probed by photoemission ($\sim$5 nm). In the case of the O 1s photoemission line (Fig. 2e), both samples show rather broad spectra: the results of a fitting procedure (reported in Fig. 2e) clearly indicate the presence of a peak at 530.3 eV distinctive of lattice oxygen in iron oxides, and two other peaks, at 532.0 eV and 533.5 eV respectively, which are compatible with the presence of different kinds of hydroxyls.[52] Therefore, the surface and the interfaces of the FeOx–MNPs are hydroxylated and strongly interacting with water. The hydroxylated surface of FeOx–MNPs contributes to their stability in bidistilled water during and after the laser ablation synthesis.

Magnetic characterization

The strong magnetic character of FeOx–MNPs can be qualitatively evidenced by simply placing a NdFeB magnet in proximity of the solutions for overnight: as shown in Fig. 3a, the particles respond to the applied field gradient. The magnetic properties of the sample were quantitatively investigated both in solution and as dry powders. Zero field cooling/field cooling (ZFC/FC) magnetization curves measured with a field of 50 Oe (Fig. 3b) indicated that thermal irreversibility starts to develop at temperatures larger than the room temperature and that a large distribution of energy barrier for the magnetization reversal occurs, as indeed expected on the basis of size distribution observed by TEM. The comparison of measurements carried out on liquid solutions and on dry powders did not evidence any relevant difference, therefore suggesting that dipolar interactions amongst particles are negligible. It is worthwhile to note that no evidence of the Verwey transition, characteristic of magnetite, is observed in the investigated temperature range. This is an orthorhombic to cubic structural transition occurring at ca. 120–125 K which is expected to produce a sharp increase of the magnetic moment.[53] Possibly, the absence of the Verwey
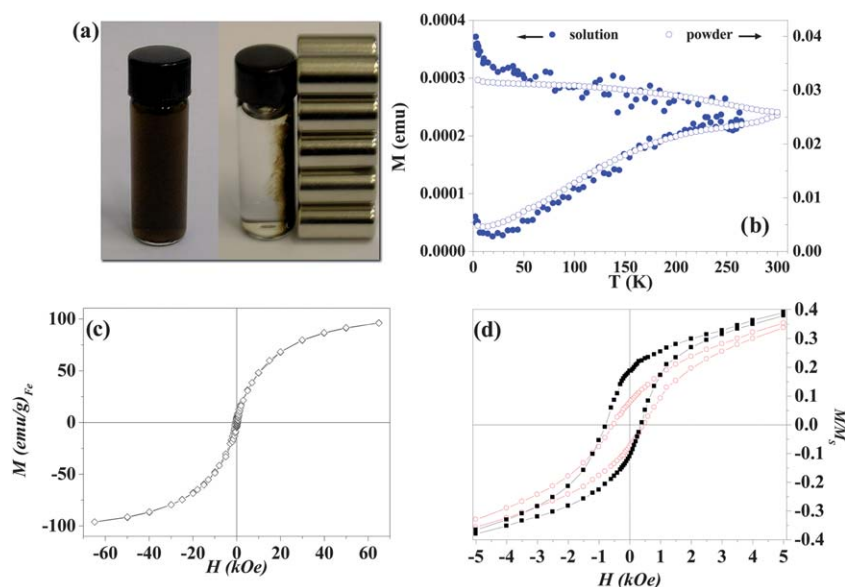
Fig. 3 Magnetic characterization of FeOx–MNPs: (a) the migration of FeOx–MNPs after overnight application of NdFeB magnets is shown in the figure; (b) temperature dependence of the ZFC/FC magnetization under $H = 50$ Oe measured for the solution (filled symbols) and dry powder (open symbols); the measurements of the solution was stopped at 265 K to avoid the melting of the solution. (c) ZFC hysteresis cycle at 2.5 K; (d) magnification of the hysteresis cycles carried out at 2.5 K after zero field cooling (ZFC—red hollow circles) and cooling in a 5 T magnetic field (FC5T—black squares); the two curves were normalized to the saturation values obtained as described in the text.

signature can be ascribed to the very small size of the actual crystalline domains. Indeed it is known that at the nanoscale, below *ca.* 50 nm, the transition temperature is size dependent, strongly decreasing with the average size, and can even not be observed in the case of particles with a size of the order of 5 nm or less.[54]

According to ZFC/FC measurements, non-zero coercivity (30 Oe) and low reduced remnant magnetization, M_0/M_{50kOe} (0.02), are observed in the hysteresis loop at room temperature, meaning that a fraction of FeOx–MNPs are still blocked. This can be due to a large magnetic anisotropy due to the exchange interactions between the magnetic Fe_3O_4 and the antiferromagnetic α-Fe_2O_3 nanodomains that are present in our FeOx–MNPs, as indicated by XRD analysis. However, another reason could be the presence of large nanoparticles in the tail of the size distribution measured by TEM analysis. In any case, this feature can be of interest for applications like magnetic hyperthermia induced by alternate magnetic fields because both the hysteresis loss and the reorientation heating mechanisms can be activated, by tuning the applied frequency.[8,55]

In order to inquire the presence of exchange anisotropy due to the coexistence of magnetic and antiferromagnetic domains in close proximity, hysteresis cycles at low temperature (2.5 K) were carried out after the sample was cooled down in zero field (ZFC) or in a 5 T static field (FC5T) (Fig. 3c and d). In both loops the sample magnetization did not reach saturation, due to surface spin canting and/or to the presence of antiferromagnetic domains. The saturation magnetization was evaluated by extrapolating the M values for $1/H \rightarrow 0$ and was found to be 110.5 emu g^{-1} of total iron. Taking into account the composition as obtained from Rietveld analysis of X-ray pattern, this value corresponds to *ca.* 80 emu g^{-1} for our FeOx–MNPs. This value is remarkably high for iron oxide nanoparticles, suggesting a high

crystalline quality of the synthesized nanomaterials. Large magnetization is important for the application of MNPs in cell sorting and cell manipulation, in magnetic induction hyperthermia, in MPI, but it is also of paramount importance for the use of MNPs as MRI contrast agents because the spin–spin relaxation time depends on the magnetic moment of nanoparticles.[5,8,56] The coercive field observed in the ZFC loop is *ca.* 500 Oe which is what commonly observed for magnetite nanoparticles. The reduced remnant magnetization is 0.10, a value much lower than that expected for an assembly of blocked single domain FeOx–MNPs (0.5 or 0.66 for uniaxial or cubic magnetic anisotropy, respectively),[57] pointing out the presence of an antiferromagnetic non-saturated phase (hematite) and the polycrystalline character of the sample. As shown in Fig. 3d, the FC5T hysteresis cycle is significantly shifted to negative fields, and presents a larger coercive field and remnant magnetization than the ZFC cycle: the shift evaluated as the half-sum between the positive and negative coercivities is 200 Oe, the average coercive field is 580 Oe and the reduced remanences are 0.23 and 0.14 for positive and negative magnetizations, respectively. Such behaviour is characteristic of exchange bias systems where ferrimagnetic/antiferromagnetic interfaces occur, and therefore well agree with the presence of magnetite and hematite nanodomains in the same polycrystalline nanoparticle.
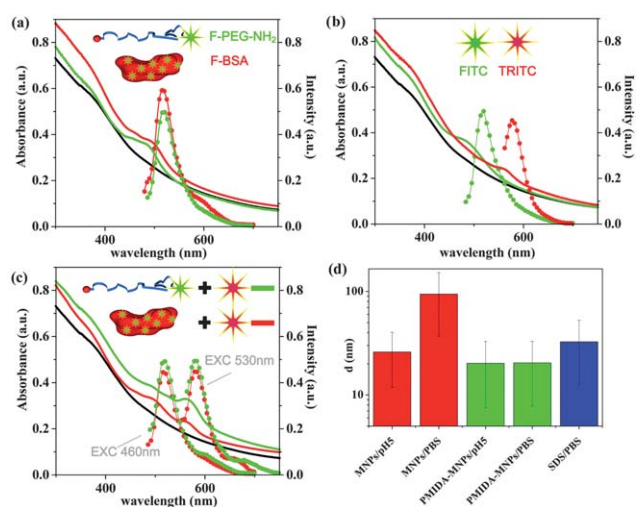
FeOx–MNPs functionalization

Functionalization of FeOx–MNPs obtained by LASiS can occur by inserting the ligands after the synthesis because the surface charge of the colloidal system prevents particles aggregation without the need for interfering stabilizing molecules, similarly to what reported for noble metal nanoparticles obtained by LASiS.[34–36]

The feasibility of MNPs conjugation after the synthetic procedure was investigated by using four different types of molecules composed by a coordination function and an optical active moiety. The molecules are fluorescein-bovine serum albumin (F-BSA), amine terminated fluorescein-poly-ethyleneglycol (F–PEG–NH$_2$) and fluorescein or tetrame-thylrhodamine isothiocyanate (FITC or TRITC) and with an effective stabilizer for physiological environments like N-phos-phonomethyl iminodiacetic acid (PMIDA).[58] The functionali-zation procedure consisted in the incubation of the FeOx–MNPs at room temperature for 24 hours with the ligand solutions. By UV-visible and fluorescence spectroscopy, we tested conjugation both in acidic (pH 4) and basic (pH 9) conditions but we generally observed better conjugation efficiency after incubation at acidic pH. This finding can be the effect of the good dispersion of FeOx–MNPs at pH 4, in contrast with the trend to agglom-eration observed at pH 9 that is characteristic of iron oxides in aqueous solutions.[4] After the incubation, excess ligands were washed multiple times with water and with phosphate buffer saline (PBS) solutions by centrifugation. We washed the func-tionalised FeOx–MNPs with PBS because it is well known in the literature that weakly bound ligands are readily displaced from the surface of iron oxide nanoparticles in physiological medium by phosphate groups.[3,4,11,12] Therefore, we are confident that only strongly bound ligands overcame our washing procedures with PBS.

BSA can be seen as a polydentate and polyfunctional ligand capable of coordinating FeOx–MNPs by carboxylic groups and amine groups.[59,60] UV-visible and fluorescence spectroscopy provided clear indications of the presence of F-BSA coating on FeOx–MNPs after the washing procedure (Fig. 4a). By exploit-ing the intense absorption of the fluorescein moiety in F-BSA (according to the datasheet of the F-BSA, 10 fluorescein mole-cules are present on average per BSA molecule) we evaluated that 2.3 nanomoles of F-BSA per mg of Fe were present after the purification step. Further confirmation of the coating of FeOx–MNPs with BSA was obtained by FTIR measurements that allowed the detection of the two intense Amide I and Amide II bands centered at approximately 1660 and 1550 cm^{-1} charac-teristic of albumin (see Fig. S1a in the ESI†).[59,60]

Alkylamines have been frequently used for the stabilization of FeOx–MNPs in aqueous solution,[4] hence we tested the conju-gation of FeOx–MNPs with a fluorescent alkylamine like F–PEG–NH$_2$. Similarly to what observed for BSA, we found that FeOx–MNPs were efficiently coated by F–PEG–NH$_2$, as assessed by UV-visible and fluorescence spectroscopy (Fig. 4a) and by FTIR analysis, where we detected the C–O stretching bands in the 1100–1000 cm^{-1} range (see Fig. S1b in the ESI†). By UV-visible spectroscopy, we evaluated that 20.6 nanomoles of F–PEG–NH$_2$ per mg of Fe were present after the purification step.

Isothiocyanates can undergo a slow reaction with nucleophilic oxygen atoms like those present on the surface of hydroxylated iron oxide nanoparticles,[10,61] hence the NCS group can be an alternative to other ligands based on ammonium, carboxylic or phosphonate groups that prevalently coordinate surface metal atoms. However, at pH 4, this reaction is not favoured. On the other hand, the thiocyanate group is well known for its coordi-nating ability of metal ions that offer a second opportunity for

Fig. 4 (a) UV-visible spectra of non-functionalized FeOx–MNPs (black line), FeOx–MNPs conjugated with F-BSA (red line) and F–PEG–NH$_2$ (green line). The absorption band of fluorescein at 490 nm is evident in both cases. The dotted green lines are the corresponding fluorescence spectra. (b) UV-visible spectra of non-functionalized FeOx–MNPs (black line), FeOx–MNPs conjugated with FITC (green line) and TRITC (red line) with the relative fluorescence emission spectra (dotted lines). The absorption bands of fluorescein at 490 nm and of rhodamine at 560 nm are evident in both cases. (c) UV-visible (straight lines) and fluorescence (dotted lines, excitation at 460 nm or 530 nm) spectra of FeOx–MNPs after sequential functionalization with F-BSA and TRITC (red lines) or with F–PEG–NH$_2$ and TRITC (green lines). (d) Average size and relative standard deviation of FeOx–MNPs at pH 4 and in PBS solutions measured by DLS.

the binding of FITC and TRITC to the surface of FeOx–MNPs. In fact, the successful coating of FeOx–MNPs with FITC and TRITC was assessed by UV-visible and fluorescence spectros-copy (as can be clearly seen in Fig. 4b). By UV-visible spec-troscopy, we evaluated that ca. 12.9 nanomoles of FITC/TRITC per mg of Fe were present after the purification step.

Since ligands are added to FeOx–MNPs after the synthetic procedure, the multifunctionalization with molecules bearing different coordinating ends is possible. We verified the feasibility of the multifuctionalization by the sequential coordination of F-BSA/FeOx–MNPs and F–PEG–NH$_2$/FeOx–MNPs with TRITC, exploiting the different site selectivity of these ligands. In order to avoid the eventuality of FeOx–MNPs surface satu-ration with phosphate from the PBS solution, the intermediate products consisting of F-BSA/FeOx–MNPs and F–PEG–NH$_2$/FeOx–MNPs were obtained by washing excess F-BSA and F–PEG–NH$_2$ with bidistilled water instead of PBS and then restoring the pH 4 after washing. Both the UV-visible and the fluorescence analysis confirmed that the sequential multi-functionalization successfully occurred (Fig. 4c). This finding can be indicative that the isothiocyanate derivatives followed a different coordinating path with respect to the amine derivative and to BSA, as discussed above.

Coordination of FeOx–MNPs with PMIDA takes place readily due to the high affinity of phosphate groups with iron oxides, as was confirmed by the FTIR spectrum of conjugated FeOx–MNPs (see Fig. S1c in the ESI†). The two carboxylic groups present in the PMIDA molecule confer high stability to

FeOx–MNPs in PBS medium and offer the opportunity for their bioconjugation by reaction with amines after activation of carboxylic groups, as reported in the valuable work of Das and coworkers.[58] We verified the excellent time stability of PMIDA coated FeOx–MNPs in PBS by dynamic light scattering (DLS) measurements. The aggregation of FeOx–MNPs in physiological medium is a well known phenomenon observed also in some commercially available ultrasmall superparamagnetic iron oxide particles that conflicts with the real applicability of MNPs *in vivo*. By DLS analysis we observed that the average size of unprotected FeOx–MNPs at pH 4 is of 26 nm, while the same particles after 24 hours in PBS have an average size of 94 nm (Fig. 4d). Similar results were found for FeOx–MNPs coated with F-BSA, F–PEG–NH$_2$, FITC or TRITC. On the contrary, by performing the DLS measurement on PMIDA/FeOx–MNPs we found an average size of 20 nm at pH 4 as well as in PBS solution. The values measured by DLS were in close agreement with what observed by TEM on the same samples. These results may be indicative that a complete coating of particles surface and a modification of FeOx–MNPs surface charges were achieved only in the case of PMIDA/FeOx–MNPs. This is a confirmation of the superior conjugation ability of phosphate groups in comparison to other ligands, and that the stabilization mechanism of PMIDA in PBS, based on the electrostatic repulsion due to the de-protonation of the carboxylic ends in basic environment, is much more efficient in comparison to the other ligands.

We also found that FeOx–MNPs are stable in PBS solution when in the presence of sodium dodecyl sulfate (SDS) at a concentration lower than the critical micellar concentration. In this case the average size obtained by DLS analysis was *ca.* 30 nm. This is especially interesting when functionalization of FeOx–MNPs by silanization or polymer encapsulation in aqueous solution is desired.[4,10] Therefore, the functionalization of FeOx–MNPs obtained by LASiS can take place also with the same methods previously reported for iron oxide nanoparticles obtained by wet chemistry synthesis.

Macrophage labelling and manipulation

Since FeOx–MNPs with size in the range of tens to hundreds of nanometres are readily uptaken by macrophages cells, have a strong magnetic response and are efficient heaters for magnetic hyperthermia,[3–5,8,10] we tested the capability of FeOx–MNPs to be uptaken by macrophage cells. Macrophages have the ability of infiltrating and accumulating in a variety of lesions like wounds, atherosclerosis plaques and deep cancerous tissues that are not reachable by EPR effects.[4,16–18,62] Therefore, macrophage cells can act as efficient and selective carriers of multifunctional FeOx–MNPs to the desired sites for a variety of applications like, for instance, wound cicatrization or cancer therapy by magnetic hyperthermia.[4] Moreover, fluorescent FeOx–MNPs can be used for the multimodal imaging of lesions by magnetic resonance and fluorescence imaging,[3,5,11,62] that is useful because MRI has a relatively low spatial resolution and cannot be used in the intrasurgical stage, contrary to fluorescence.[3,5,11,62]

While the loading of cells with MNPs has been frequently reported in the literature,[63] the loading of macrophage cells with magneto-fluorescent particles is less frequent. In our experiments, fluorescein conjugated FeOx–MNPs (F–PEG–NH$_2$/MNPs) were first incubated with U937 cells, differentiated into macrophages by exposure to PMA, at 37 °C for 4 hours and then thoroughly washed in order to remove excess particles (see the Experimental methods for details). After incubation and washing procedures, we assayed the uptake of particles by flow cytometry and confocal microscopy (Fig. 5). A clear fluorescence signal due to the fluorescein adsorbed on FeOx–MNPs was detected in both
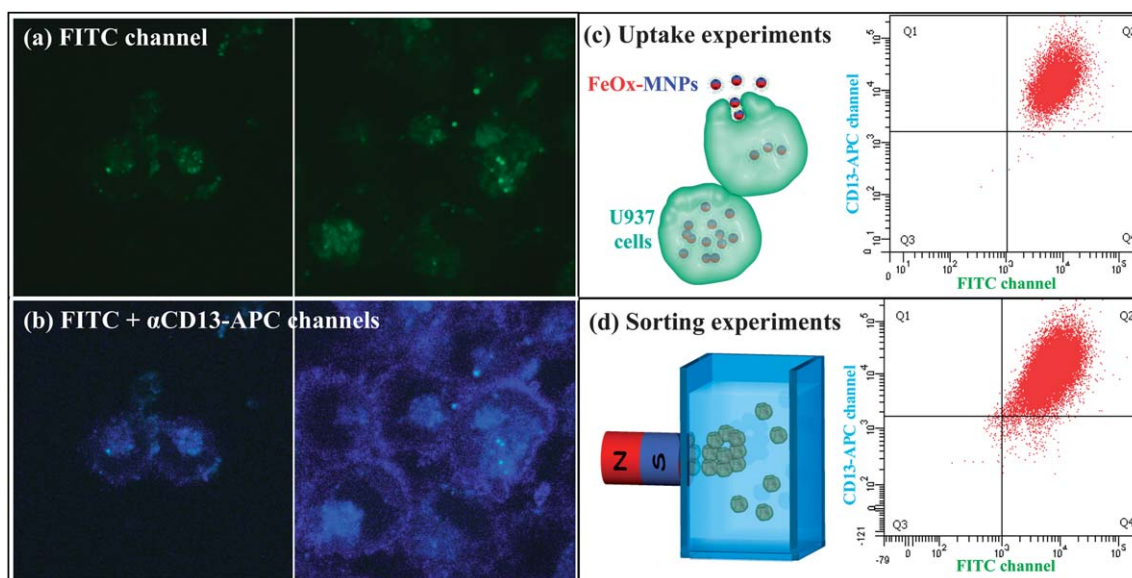
Fig. 5 Two representative confocal microscope images of macrophages after incubation with F–PEG–NH$_2$/FeOx–MNPs and staining with αCD13–APC. (a) FITC fluorescence channel only; (b) merged images of αCD13–APC and FITC fluorescence channels. Macrophages, after incubation with FITC-labelled MNPs and staining with αCD13–APC, were separated by a magnet. Cells were then analyzed by flow cytometry before (c) and after (d) the sorting experiments. (c) Cytofluorimetric analysis of macrophages showing efficient phagocytosis of fluorescent MNPs (FITC labelled) by all cells analysed; (d) cytofluorimetric analysis of positively sorted cells.
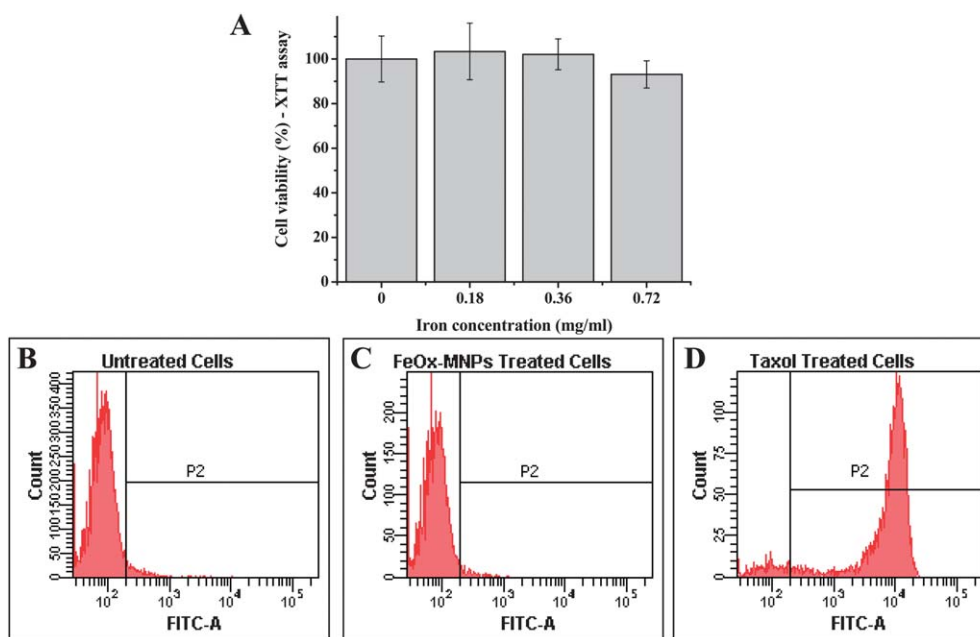
Fig. 6 a) XTT assay of cell viability: U937 differentiated cells were incubated for 4 h at 37 °C with FeOx–MNPs at an iron concentration of 0.18, 0.36 and 0.72 mg ml^{-1} and the cell viability was measured after 20 h. Evaluation of cell apoptosis: U937 differentiated cells were incubated for 4 h at 37 °C with FeOx–MNPs; then cell apoptosis was assessed after 20 h by flow cytometry using the human Annexin V protocol (b: U937 untreated cells, c: FeOx–MNPs treated cells; d: Taxol treated cells used as positive control of apoptosis).

cases (Fig. 5). Moreover, macrophage cells were stained with antiCD13–APC labelled antibody that is a marker selective for the membrane of macrophage cells and provides a good contrast for the visualization of cell walls. Confocal microscopy analysis emphasized that fluorescence from fluorescein is observed in the central part of the cells, as expected after phagocytosis of particles, while the CD13–APC signal is collected principally from the cell walls as expected for this type of label (Fig. 5a and b). Flow cytometry indicated that more than 95% of macrophage cells had a magnetic-fluorescent payload after incubation with F–PEG–NH$_2$/MNPs (Fig. 5c).

Macrophage cells with a magnetic payload can be sorted in order to select the most effective population for therapeutic and diagnostic purposes. Therefore we tested the possibility of manipulating macrophages with an external magnetic field by a cell sorting experiment carried out at 4 °C with a magnetic trap based on a NdFeB magnet (Fig. 5d). The cells separated by the magnetic trap after 10 minutes and the cells not trapped by the magnet were assayed by flow cytometry and the double fluorescence signal associated to MNPs and CD13 staining was quantitatively analyzed. We found that the 95% of the macrophages were effectively captured by the magnetic trap after only 10 minutes of exposure (Fig. 5d). The flow cytometry shows that lower fluorescence intensity in the fluorescein channel is measured for non-sorted cells (Fig. S2 in the ESI†), in agreement with the presence of a lower FeOx–MNPs payload in these cells. These data show that macrophage cells loaded with fluorescent FeOx–MNPs can be effectively sorted and manipulated by means of a magnetic field.

Moreover, we investigated the cell viability and the presence of apoptosis events after exposure to FeOx–MNPs. Macrophage viability after FeOx–MNPs incorporation was assessed by the

XTT assay that measures the activity of intracellular reductase enzymes. U937 differentiated cells were incubated for 4 h at 37 °C with FeOx–MNPs at a Fe concentration of 0.18, 0.36 and 0.72 mg ml^{-1} and the cell viability was measured after 20 hours analyzing XTT reduction with a microplate reader. As shown in Fig. 6a, no influence of FeOx–MNPs on the cell viability was evidenced by the XTT assay.

We also investigated the induction of apoptosis events in U937 differentiated cells exposed to FeOx–MNPs for 4 hours at a Fe concentration of 0.36 mg ml^{-1}. Cells were analysed 2 hours and 20 hours after the removal of excess FeOx–MNPs by the human Annexin V-FITC protocol that is specific for the phosphatidylserine expression on the outer leaflet of the cell membrane. Flow cytometry analysis after 2 hours and after 20 hours demonstrated that no apoptotic events were present (Fig. 6b–d).

Conclusions

The synthesis of multifunctional magnetic nanoparticles is a topic of great interest for nanomedicine applications. Here we presented a new method for obtaining FeOx–MNPs in water solution based on the Laser Ablation Synthesis in Solution (LASiS). LASiS is a top-down "green" technique for obtaining colloidal solutions of nanoparticles without chemicals and with limited manual operation. A variety of complementary investigation techniques were used for the characterization of our FeOx–MNPs. The results indicated that FeOx–MNPs have nanometric size, a polycrystalline structure composed prevalently of magnetite with a minor fraction of hematite and a significant hydroxylation of interfaces. Magnetic characterization showed that FeOx–MNPs have a saturation magnetization of *ca.* 80 emu g^{-1}, higher than values usually reported for

MNPs with similar size and composition. The unusual magnetic properties observed on our FeOx–MNPs can be ascribed to the coexistence of ferrimagnetic (magnetite) and antiferromagnetic (hematite) phases in the same polycrystalline structure. The feasibility of functionalization and sequential multi-functionalization of FeOx–MNPs with carboxylated phosphonates, fluorescent alkylamines, fluorescent isothiocyanates and bovine serum albumin were demonstrated. In particular, PMIDA and SDS resulted as excellent stabilizers of FeOx–MNPs in physiological medium and can offer the opportunity for further functionalization of particles surface. FeOx–MNPs did not show any cytotoxic effect and do not induce apoptosis in our experimental conditions. Fluorescent MNPs were used for uptake and manipulation studies with macrophage cells. The multifunctionality of FeOx–MNPs was exploited for detecting the uptake in U937 macrophage cells by fluorescence microscopy and by flow cytometry and for the quantitative assay of cell sorted by a magnetic trap. In this way we obtained vehicles that can autonomously transport theranostic agents into tissues or lesions that are hardly reached by the haematic flux.

Acknowledgements

References

1 H. Zeng and S. Sun, *Adv. Funct. Mater.*, 2008, **18**, 391–400.
2 A. H. Lu, E. L. Salabas and F. Schuth, *Angew. Chem., Int. Ed.*, 2007, **46**, 1222–1245.
3 J. Gao, H. Gu and B. Xu, *Acc. Chem. Res.*, 2009, **42**, 1097–1107.
4 A. K. Gupta and M. Gupta, *Biomaterials*, 2005, **26**, 3995–4021.
5 H. B. Na, I. C. Song and T. Hyeon, *Adv. Mater.*, 2009, **21**, 2133–2148.
6 W. Lin, T. Hyeon, G. M. Lanza, M. Zhang and T. J. Meade, *MRS Bull.*, 2009, **34**, 441–448.
7 B. Gleich and J. Weizenecker, *Nature*, 2005, **435**, 1214–1217.
8 S. Mornet, S. Vasseur, F. Grasset and E. Duguet, *J. Mater. Chem.*, 2004, **14**, 2161–2175.
9 D. H. Kim, E. A. Rozhkova, I. V. Ulasov, S. D. Bader, T. Rajh, M. S. Lesniak and V. Novosad, *Nat. Mater.*, 2009, **9**, 165–171.
10 A. G. Roca, R. Costo, A. F. Rebolledo, S. Veintemillas-Verdaguer, P. Tartaj, T. Gonzalez-Carreno, M. P. Morales and C. J. Serna, *J. Phys. D: Appl. Phys.*, 2009, **42**, 224002–224012.
11 A. Quarta, R. Di Corato, L. Manna, S. Argentiere, R. Cingolani, G. Barbarella and T. Pellegrino, *J. Am. Chem. Soc.*, 2008, **130**, 10545–10555.
12 D. Shi, H. S. Cho, Y. Chen, H. Xu, H. Gu, J. Lian, W. Wang, G. Liu, C. Huth and L. Wang, *Adv. Mater.*, 2009, **21**, 2170–2173.
13 M. Liong, J. Lu, M. Kovochich, T. Xia, S. G. Ruehm, A. E. Nel, F. Tamanoi and J. I. Zink, *ACS Nano*, 2008, **2**, 889–896.
14 J. H. Park, G. von Maltzahn, L. Zhang, M. P. Schwartz, E. Ruoslahti, S. N. Bhatia and M. J. Sailor, *Adv. Mater.*, 2008, **20**, 1630–1635.
15 Y. Zhang, N. Kohler and M. Zhang, *Biomaterials*, 2002, **23**, 1553–1561.
16 E. K. U. Larsen, T. Nielsen, T. Wittenborn, H. Birkedal, T. Vorup-Jensen, M. H. Jakobsen, L. Østergaard, M. R. Horsman, F. Besenbacher and K. A. Howard, *ACS Nano*, 2009, **3**, 1947–1951.
17 M. K. Yu, Y. Y. Jeong, J. Park, S. Park, J. W. Kim, J. J. Min, K. Kim and S. Jon, *Angew. Chem., Int. Ed.*, 2008, **47**, 5362–5365.
18 L. L. Ma, M. D. Feldman, J. M. Tam, A. S. Paranjape, K. K. Cheruku, T. A. Larson, J. O. Tam, D. R. Ingram, V. Paramita and J. W. Villard, *ACS Nano*, 2009, **3**, 2686–2696.
19 M. Hoehn, E. Küstermann, J. Blunk, D. Wiedermann, T. Trapp, S. Wecker, M. Föcking, H. Arnold, J. Hescheler and B. K. Fleischmann, *Proc. Natl. Acad. Sci. U. S. A.*, 2002, **99**, 16267–16272.
20 R. Narain, M. Gonzales, A. S. Hoffman, P. S. Stayton and K. M. Krishnan, *Langmuir*, 2007, **23**, 6299–6304.
21 S. Kalele, R. Narain and K. M. Krishnan, *J. Magn. Magn. Mater.*, 2009, **321**, 1377–1380.
22 V. S. Coker, N. D. Telling, G. van der Laan, R. A. Pattrick, C. I. Pearce, E. Arenholz, F. Tuna, R. E. Winpenny and J. R. Lloyd, *ACS Nano*, 2009, **3**, 1922–1928.
23 L. Wang, Z. Yang, Y. Zhang and L. Wang, *J. Phys. Chem. C*, 2009, **113**, 3955–3959.
24 B. W. Muir, B. A. Moffat, P. Harbour, G. Coia, G. Zhen, L. Waddington, J. Scoble, D. Krah, S. H. Thang and Y. K. Chong, *J. Phys. Chem. C*, 2009, **113**, 16615–16624.
25 X. Sun, C. Zheng, F. Zhang, Y. Yang, G. Wu, A. Yu and N. Guan, *J. Phys. Chem. C*, 2009, **113**, 16002–16008.
26 S. Ge, X. Shi, K. Sun, C. Li, C. Uher, J. R. Baker,Jr, M. M. B. Holl and B. G. Orr, *J. Phys. Chem. C*, 2009, **113**, 13593–13599.
27 Q. A. Pankhurst and R. J. Pollard, *Phys. Rev. Lett.*, 1991, **67**, 248–250.
28 C. J. Serna, F. Bødker, S. Mørup, M. P. Morales, F. Sandiumenge and S. Veintemillas-Verdaguer, *Solid State Commun.*, 2001, **118**, 437–440.
29 A. Millan, A. Urtizberea, N. J. O. Silva, F. Palacio, V. S. Amaral, E. Snoeck and V. Serin, *J. Magn. Magn. Mater.*, 2007, **312**, L5–L9.
30 A. G. Roca, J. F. Marco, M. del Puerto Morales and C. J. Serna, *J. Phys. Chem. C*, 2007, **111**, 18577–18584.
31 F. Hu, K. W. MacRenaris, E. A. Waters, T. Liang, E. A. Schultz-Sikma, A. L. Eckermann and T. J. Meade, *J. Phys. Chem. C*, 2009, **113**, 20855–20860.
32 K. Buyukhatipoglu, T. A. Miller and A. Morss Clyne, *J. Nanosci. Nanotechnol.*, 2009, **9**, 6834–6843.
33 K. Buyukhatipoglu and A. Morss Clyne, *J. Nanopart. Res.*, 2010, **12**, 1495–1508.
34 V. Amendola and M. Meneghetti, *Phys. Chem. Chem. Phys.*, 2009, **11**, 3805–3821.
35 V. Amendola and M. Meneghetti, *J. Mater. Chem.*, 2007, **17**, 4705–4710.
36 V. Amendola and M. Meneghetti, *J. Phys. Chem. C*, 2009, **113**, 4277–4285.
37 S. Enzo, S. Polizzi and A. Benedetti, *Z. Kristallogr.*, 1985, **170**, 275–287.
38 P. Riello, P. Canton and G. Fagherazzi, *J. Appl. Crystallogr.*, 1998, **31**, 78–82.
39 G. Compagnini, A. A. Scalisi and O. Puglisi, *Phys. Chem. Chem. Phys.*, 2002, **4**, 2787–2791.
40 F. Mafune, J. Kohno, Y. Takeda, T. Kondow and H. Sawabe, *J. Phys. Chem. B*, 2000, **104**, 9111–9117.
41 O. K. Borggaard, *Eur. J. Soil Sci.*, 1976, **27**, 478–486.
42 D. Bersani, P. P. Lottici and A. Montenero, *J. Raman Spectrosc.*, 1999, **30**, 355–360.
43 W. Wang, J. Y. Howe and B. Gu, *J. Phys. Chem. C*, 2008, **112**, 9203–9208.
44 J. Tang, M. Myers, K. A. Bosnick and L. E. Brus, *J. Phys. Chem. B*, 2003, **107**, 7501–7506.
45 I. Chamritski and G. Burns, *J. Phys. Chem. B*, 2005, **109**, 4965–4968.
46 S. Nasrazadani, *Corros. Sci.*, 1997, **39**, 1845–1859.
47 S. Nasrazadani and H. Namduri, *Spectrochim. Acta, Part A*, 2006, **61**, 565–571.
48 S. Nasrazadani and A. Raman, *Corros. Sci.*, 1993, **34**, 1355–1365.
49 I. V. Chernyshova, M. F. Hochella Jr and A. S. Madden, *Phys. Chem. Chem. Phys.*, 2007, **9**, 1736–1750.
50 A. Corrias, G. Mountjoy, D. Loche, V. Puntes, A. Falqui, M. Zanella, W. J. Parak and M. F. Casula, *J. Phys. Chem. C*, 2009, **113**, 18667–18675.
51 A. P. Grosvenor, B. A. Kobe, M. C. Biesinger and N. S. McIntyre, *Surf. Interface Anal.*, 2004, **36**, 1564–1574.

52 T. Kendelewicz, P. Liu, C. S. Doyle, G. E. Brown, Jr, E. J. Nelson and S. A. Chambers, *Surf. Sci.*, 2000, **453**, 32–46.
53 F. Walz, *J. Phys.: Condens. Matter*, 2002, **14**, R285–R340.
54 G. F. Goya, T. S. Berquo, F. C. Fonseca and M. P. Morales, *J. Appl. Phys.*, 2003, **94**, 3520.
55 S. A. Rovers, L. A. M. van der Poel, C. H. J. T. Dietz, J. J. Noijen, R. Hoogenboom, M. F. Kemmere, K. Kopinga and J. T. F. Keurentjes, *J. Phys. Chem. C*, 2009, **113**, 14638–14643.
56 H. M. Joshi, Y. P. Lin, M. Aslam, P. V. Prasad, E. A. Schultz-Sikma, R. Edelman, T. Meade and V. P. Dravid, *J. Phys. Chem. C*, 2009, **113**, 17761–17767.
57 J. L. Dormann, D. Fiorani and E. Tronc, *Adv. Chem. Phys.*, 1997, **98**, 283–494.

58 M. Das, D. Mishra, P. Dhak, S. Gupta, T. K. Maiti, A. Basak and P. Pramanik, *Small*, 2009, **5**, 2883–2893.
59 C. H. Yu, A. Al-Saadi, S. Shih, L. Qiu, K. Y. Tam and S. C. Tsang, *J. Phys. Chem. C*, 2009, **113**, 537–543.
60 M. Mikhaylova, D. O. K. Kim, C. C. Berry, A. Zagorodni, M. Toprak, A. S. G. Curtis and M. Muhammed, *Chem. Mater.*, 2004, **16**, 2344–2354.
61 Y. Iwakura and H. Hokada, *Can. J. Chem.*, 1962, **40**, 2369–2375.
62 J. R. McCarthy and R. Weissleder, *Adv. Drug Delivery Rev.*, 2008, **60**, 1241–1251.
63 G. Frasca, F. Gazeau and C. Wilhelm, *Langmuir*, 2009, **25**, 2348–2354.